Tailoring the Bactericidal Activity of Ag Nanoparticles/α-Ag₂WO₄ Composite Induced by Electron Beam and Femtosecond Laser Irradiation: Integration of Experiment and Computational Modeling

Nadia G. Macedo,[†] Thales R. Machado,[†] Roman A. Roca,[†] Marcelo Assis,[†] Camila Cristina Foggi,[†] Verónica Puerto-Belda,[‡] Gladys Mínguez-Vega,[‡] André Rodrigues,[§] Miguel A. San-Miguel,[§] Eloisa Cordoncillo,[∥] Héctor Beltrán-Mir,[∥] Juan Andrés,*,[⊥] and Elson Longo[†]

[†]CDMF, LIEC, Federal University of São Carlos (UFSCar), P.O. Box 676, São Carlos, São Paulo 13565-905, Brazil
[‡]GROC·UJI, Institut de Noves Tecnologies de la Imatge (INIT), [∥]Department of Inorganic and Organic Chemistry, [⊥]Department of Analytical and Physical Chemistry, University Jaume I (UJI), Castelló 12071, Spain
[§]Department of Physical Chemistry, Institute of Chemistry, State University of Campinas, Campinas, São Paulo 13083-970, Brazil

Ⓢ Supporting Information

ABSTRACT: In nanotechnology research, significant effort is devoted to fabricating patterns of metallic nanoparticles on the surfaces of different semiconductors to find innovative materials with favorable characteristics, such as antimicrobial and photocatalytic properties, for novel applications. We present experimental and computational progress, involving a combined approach, on the antimicrobial activity against methicillin-resistant *Staphylococcus aureus* (MRSA) of as-synthesized α-Ag₂WO₄ samples and Ag nanoparticle composites (Ag NPs)/α-Ag₂WO₄. The former included two morphologies: hexagonal rod-like (α-Ag₂WO₄-R) and cuboid-like (α-Ag₂WO₄-C), and the latter included composites formed under electron beam, Ag NPs/α-Ag₂WO₄-RE and Ag NPs/α-Ag₂WO₄-CE, and femtosecond (fs) laser irradiation, Ag NPs/α-Ag₂WO₄-RL and Ag NPs/α-Ag₂WO₄-CL. Direct observations of the arrangement of Ag NPs on the Ag NPs/α-Ag₂WO₄ composites irradiated with an electron beam and laser, through transmission electron microscopy (TEM), high-resolution TEM, energy-dispersive X-ray spectroscopy, and field-emission scanning electron microscopy, allow us to investigate the surface morphology, chemical composition, homogeneity, and crystallinity. Therefore, these experimental factors, and in particular, the facet-dependent response of Ag NPs/α-Ag₂WO₄ composites were discussed and analyzed from the perspective provided by the results obtained by first-principles calculations. On this basis, α-Ag₂WO₄-R material proved to be a better bactericidal agent than α-Ag₂WO₄-C with minimum bactericidal concentration (MBC) values of 128 and 256 μg/mL, respectively. However, the Ag NPs/α-Ag₂WO₄-CL composite is the most efficient bactericidal agent of all tested samples (MBC = 4 μg/mL). This superior performance can be attributed to the cooperative effects of crystal facets and defect engineering. These results on the synthesis and stability of the Ag NPs/α-Ag₂WO₄ composites can be used for the development of highly efficient bactericidal agents for use in environmental remediation and the potential extension of methods to produce materials with catalytic applications.

KEYWORDS: Ag nanoparticles, α-Ag₂WO₄, Ag NPs/α-Ag₂WO₄ composite, electron beam and femtosecond laser irradiation, morphology
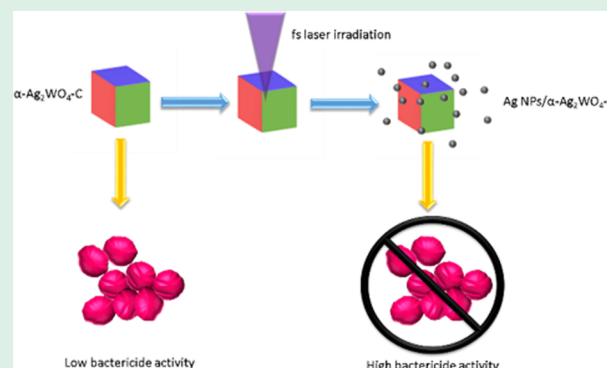
1. INTRODUCTION

Intense research activity has been devoted recently to finding active semiconductor-based materials to eradicate or degrade organic pollutants and microorganisms from various sources, such as industrial effluents, agricultural runoff, and wastewater.[1,2] This has proved to be a favorable technology, because it is found to be a nontoxic, economical, and efficient technique for the mineralization of pollutants in water.[3−5] However, the activity of semiconductor surfaces is significantly influenced, not only by the dynamics of the photogenerated holes and electrons, which need to reach the surface to be catalytically active,[6] but also the photocatalysts, which must be sensitive to visible light.

To overcome these drawbacks, an adequate alternative is to develop metal−semiconductor heterojunctions, such as those
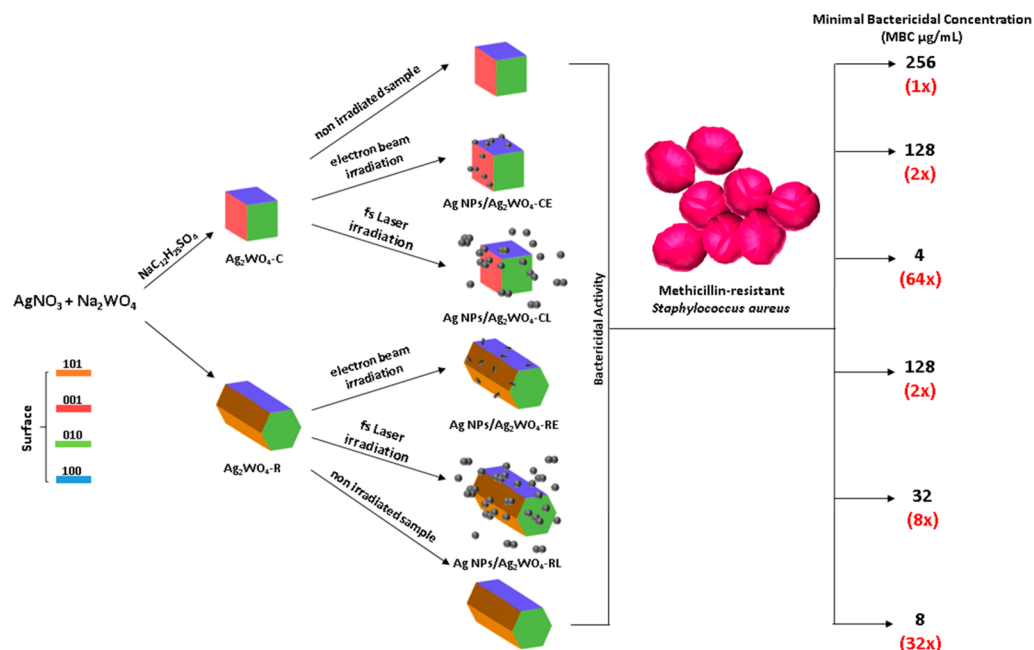
Figure 1. Schematic representation of the procedures employed to obtain Ag NPs/α-Ag$_2$WO$_4$ composites by electron beam and fs laser irradiations. Two morphologies are employed: hexagonal rod-like (α-Ag$_2$WO$_4$-R) and cuboid-like (α-Ag$_2$WO$_4$-C), which can be attained in the facile synthesis of α-Ag$_2$WO$_4$ without and with the presence of the anionic surfactant sodium dodecyl sulfate, respectively. The as-obtained Ag NPs/α-Ag$_2$WO$_4$ composites present different activities against methicillin-resistant *Staphylococcus aureus* (MRSA).

used in materials science, to yield innovative materials with enhanced or new properties and improved photocatalytic performance. The electronic structures and energy band structures of such materials are modifiable and tunable by changing their crystal structures. Their production has opened up new fields of applications, such as electrocatalysis, photocatalysis, electroanalysis, and environmental chemistry.[7] In this context, the deposition of noble nanoparticles (NPs), such as Ag, Au, Cu, and Pt onto the surface of a semiconductor, to form a metal−semiconductor composite, has been proposed as a means to produce promising materials, owing to their advantageous features related to surface plasmon resonance (SPR), additional active sites, and/or electronic traps.[8] When Ag NPs are deposited on the surface of wide-band gap photocatalysts, numerous advantages can be observed: they can (i) act as a sensitizer to extend the light absorption region by amplifying the absorption of visible light; (ii) improve the separation rate of the photogenerated holes and electrons, as well as preventing the recombination of photogenerated electrons and holes; and (iii) facilitate certain specific reactions on the surface of the semiconductor, thereby resulting in an improvement in the photocatalytic efficiency.[9,10]

In this framework, Ag NPs and their associated Ag-containing composites can be exploited as promising candidates of potent antibacterial agents, in addition to their SPR effect.[11,12] The SPR of Ag NPs is an influential phenomenon that has already been used in many applications.[13−15] The highly efficient plasmonic photocatalysts of composites such as Ag/g-C$_3$N$_4$, Ag/TiO$_2$, Ag/ZnO, Ag/AgCl, Ag/AgVO$_3$, Ag/Ag$_3$PO$_4$, Ag/BiOI, Ag/ZnTiO$_3$, Ag/ZnWO$_4$, Ag/Ag$_2$MoO$_4$, and Ag/Ag$_2$WO$_4$ have been reported, and the corresponding results indicated that the Ag decoration dramatically enhances the photocatalytic performance of the pure photocatalyst via the SPR effect.[10,15−21]

Metal NPs decorated on the surface of semiconductors are prepared mainly through two methods, distinguishable by the sources of the metal NPs. One is from colloid, and the other is from the reduction of metal salt.[8] However, one of the prime research focuses in this area is to find a green, cost-effective, and sustainable method for the fabrication of metal NPs/semiconductor composites. In contrast to these traditional synthesis methods, two particularly effective, fast, and clean methods emerge: electron beam irradiation inside a scanning electron microscope (SEM) or transmission electron microscope (TEM) and femtosecond (fs) laser irradiation.[22,23] In this context, both the high-energy electron beam of an electronic microscope and laser light with very short pulses are known to cause ejection of material composed largely of NPs in a broad variety of targets, revealing themselves as amazing tools to produce various NPs and their compounds on the surfaces of several substrates. They are versatile and easy-to-use techniques for the preparation of such NPs and are normally performed as a one-step and one-pot synthesis, which minimizes the required amounts of solvents and precursors.[22,23]

α-Ag$_2$WO$_4$ is a semiconductor material that presents interesting and promising properties, such as photoluminescence,[24,25] photocatalysis,[26−28] gas sensing,[29−31] antimicrobial, and antifungal activities.[32−34] Our research group, by means of a combination of experimental and theoretical work, has conducted studies concerned with the growth of Ag NPs on several Ag constituent materials under exposure to electron beams using electronic microscopy, such as α-Ag$_2$WO$_4$,[32,35−40] β-Ag$_2$WO$_4$,[41,42] β-Ag$_2$MoO$_4$,[43,44] Ag$_2$CrO$_4$,[45] AgVO$_3$,[46] and Ag$_3$PO$_4$ crystals,[47] in which the nucleation of Ag NPs on the surfaces of these materials take place.[48−50] These Ag/semiconductor composites present a Schottky barrier that is generated at the interface of the Ag NPs and the semiconductor, which can effectively improve the separation efficiency of photoinduced electron−hole pairs. At the same time, Ag absorption at the surface of the semiconductor produces the SPR effect, which can significantly enhance the absorption of

visible light and improve the excitation of active charge carriers for a semiconductor photocatalyst.[51,52]

Laser irradiation is an adequate procedure to provoke localized surface modifications within well-defined regions of a wide range of semiconductors,[53,54] which allows precise control over the structure, composition, and physical properties of samples with minimal energy losses.[54] Very recently, our research group has reported four new phenomena provoked by fs laser irradiation: (i) the scaled up formation of Ag NPs on α-Ag$_2$WO$_4$ with bactericidal properties by fs laser irradiation,[40] (ii) the synthesis of metallic Bi NPs with coexisting crystallographic structures (rhombohedral, monoclinic, and cubic) on NaBiO$_3$,[55] (iii) the formation of In NPs on InP,[56] and (iv) the synthesis of Ag–Bi nanoalloys from inorganic oxide Ag$_2$WO$_4$ and NaBiO$_3$ targets.[57]

In a previous paper, we demonstrated how the control of the morphology of as-synthesized α-Ag$_2$WO$_4$ samples can be achieved in the facile synthesis of α-Ag$_2$WO$_4$ by the presence of an anionic surfactant, sodium dodecyl sulfate, to obtain two different morphologies: hexagonal rod-like (α-Ag$_2$WO$_4$-R) and cuboid-like (α-Ag$_2$WO$_4$-C), and evaluated the photocatalytic activity of both morphologies with respect to rhodamine-B.[27] α-Ag$_2$WO$_4$-C crystal presents (001), (010), and (100) exposed surfaces and the morphology of α-Ag$_2$WO$_4$-R is composed of (101), (001), and (010) surfaces. Thus, it is valuable and necessary to investigate α-Ag$_2$WO$_4$ crystals with different morphologies obtained under nearly the same conditions. In this work, we seek to fulfill three aims (Figure 1). The first and second are to report not only the key role of the morphology of the α-Ag$_2$WO$_4$ material on the generation of Ag NPs provoked by electron beam and fs laser irradiation but also the structural characteristics of the produced Ag NPs. To support this finding, detailed analyses of images obtained by advanced electron microscopy techniques, including field-emission scanning electron microscopy (FE-SEM), TEM, high-resolution TEM (HR-TEM), scanning TEM (STEM), and energy-dispersive X-ray spectroscopy (EDS) have been performed. The third objective is to demonstrate the facet-dependent response of the as-synthesized Ag NPs/α-Ag$_2$WO$_4$ composites as excellent antimicrobial agents against methicillin-resistant *Staphylococcus aureus* (MRSA) and contribute to broadening their possible applications. In addition, to rationalize and complement the experimental results, the surface structure of the different morphologies of the Ag NPs/α-Ag$_2$WO$_4$ composite was discussed and analyzed from the perspective provided by the results obtained by first-principles calculations.

2. EXPERIMENTAL PROCEDURES

2.1. Synthesis. Both the α-Ag$_2$WO$_4$-R and α-Ag$_2$WO$_4$-C samples were synthesized following the procedures previously reported by our group.[27] The Ag NPs/α-Ag$_2$WO$_4$ composites used in the bactericide tests were generated in two ways. The first method was the electron irradiation of approximately 100 g of each material sample inside a field-emission scanning electron microscope (FE-SEM) (Supra 35-VP, Carl Zeiss, Germany) with an accelerating voltage of 30 kV for a 30 min period, which yielded the Ag NPs/α-Ag$_2$WO$_4$-RE and Ag NPs/α-Ag$_2$WO$_4$-CE samples.[35] For the synthesis via laser irradiation, α-Ag$_2$WO$_4$ powders were prepared and irradiated under ambient conditions with a Ti/sapphire laser (Femtopower Compact Pro Femto Lasers), delivering pulses with a full width at half-maximum (fwhm) of 30 fs, central wavelength of 800 nm, repetition rate of 1 kHz, and maximum average energy per pulse of 0.8 mJ. In order to obtain better pulse compression on the sample, we used an acousto–optic programmable filter (DAZZLER, Faslite). A laser beam with a mean

power of 200 mW was focused onto the surface of the target powder with a spherical convex lens of 75 mm focal length in order to obtain a focal spot with a diameter of 20.6 μm fwhm. The samples were placed on the bottom of a quartz cuvette and attached to a motion-controlled two-dimensional stage, moving at a constant speed of 0.45 mm s^{-1} at the focal plane perpendicular to the laser beam. The irradiation parameter values were selected based on previously reported experiments, where the best NP growth in semiconductor networks was reported.[40] The samples yielded by this process were named Ag NPs/α-Ag$_2$WO$_4$-RL and Ag NPs/α-Ag$_2$WO$_4$-CL.

2.2. Characterization. The samples α-Ag$_2$WO$_4$-R and -C were exposed to an electron beam using an FE-SEM Supra 35-VP Carl Zeiss instrument operated at 10 kV, and their interactions with the electron beam were monitored for a certain period of time. *In situ* TEM analysis was performed using a Jeol JEM-2100F with a field-emission gun (FEG) operating at 200 kV. HR-TEM was also performed using the same microscope. The laser-irradiated samples (Ag NPs/α-Ag$_2$WO$_4$-RL and Ag NPs/α-Ag$_2$WO$_4$-CL) were also analyzed by EDS operating in STEM mode. The EDS mapping was performed using a TECNAI G2F20 transmission microscope operating in scanning mode.

2.3. Theoretical Methods. All calculations were carried out using the density functional theory, as implemented in the Vienna *Ab Initio* Simulation Package (VASP).[58] The generalized gradient approximation (GGA) was used to treat the exchange and correlation using the PBE functional. A plane-wave basis set was used to describe the valence electrons,[59] and the projector-augmented-wave method[60] was used to describe the interactions between the core and valence electrons (4d and 5s for Ag atoms, 5d and 6s for W atoms, and 2s and 2p for O atoms). An energy plane-wave cutoff of 460 eV was used to obtain convergence of at least 1 meV/atom. Brillouin zone integrations were done using converged Monkhorst–Pack grids,[61] as well as the tetrahedron method with Blochl corrections.[62] The structure was optimized with electronic and ionic convergence criteria of 10^{-6} eV and 0.005 eV Å^{-1}, respectively. The diffusion process of Ag in the system was investigated using the NEB method.[63] The atomic charges were estimated using the quantum theory of atoms in molecules (QTAIM),[64] which is a well-established tool to analyze electron density and rationalize chemical bonding. This approach is based on finding the critical points of charge density in order to divide the 3D space into volumes assigned to the different atoms. The charge associated with each atom is estimated from the integration of the charge density in the corresponding volume. Some caution must be taken when considering the absolute values of Bader charges, but they become quite convenient and useful when comparing different systems in similar situations for finding general trends. *Ab initio* molecular dynamics simulations were carried out in the canonical ensemble at 300 K. The time step was 3 fs, and a typical simulation spanned approximately 6 ps.

2.4. Antimicrobial Activity. A standard strain of MRSA obtained from the American Type Culture Collection (ATCC 33591) was used for the bactericidal tests, following the standards of the Clinical Laboratory Standards Institute (CLSI), with modifications. The bacterial inoculum was prepared as previously described.[33] The Ag$_2$WO$_4$ samples were weighed and diluted in TSB culture medium at concentrations of 2000−0.98 μg/mL and incubated with the bacterial cells for 24 h at 37 °C in a static oven. Next, 25 mL aliquots were taken from each well and placed in Petri dishes containing Mueller Hinton Agar culture medium and incubated in a static oven for 48 h at 37 °C. The positive control consisted of inoculum of MRSA without the presence of microcrystals, and the negative control consisted of culture medium without inoculum. The growth of colonies was then observed, thus determining the lowest concentration of each compound needed to eliminate the microorganism tested. The tests were performed in triplicate, on three separate occasions, to ensure the reproducibility of the results.

3. RESULTS

3.1. Ag Growth Process Induced by FE-SEM. As already explained, excess electron attachment is bound to the lattice framework and thus might penetrate it; however, the evolution
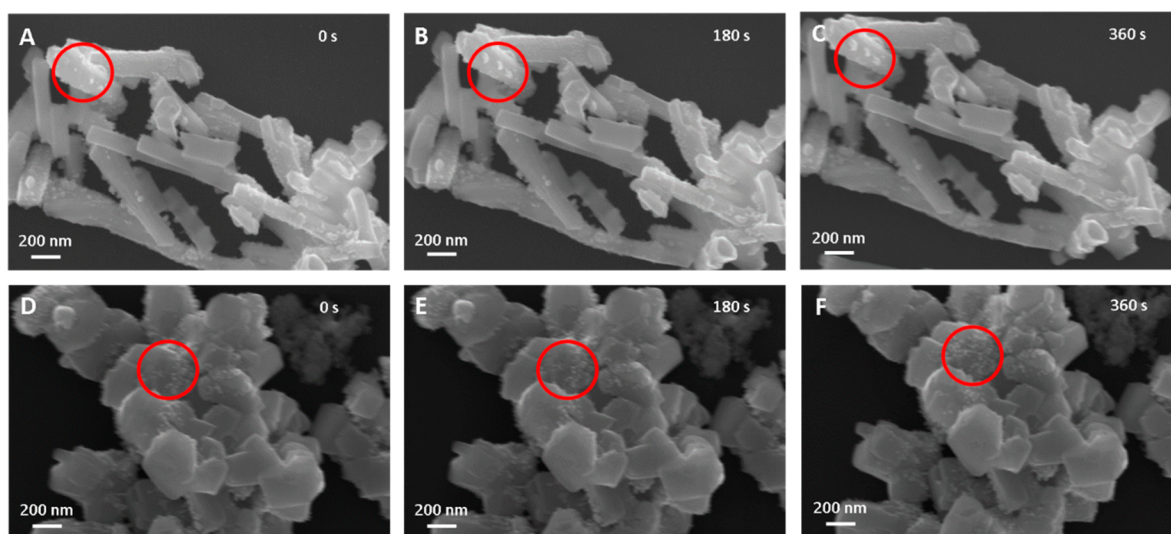
Figure 2. FE-SEM images of Ag NPs/α-Ag$_2$WO$_4$ composites within a controlled time of exposure to a 10 kV electron beam. (A−C) Ag NPs/α-Ag$_2$WO$_4$-RE; (D−F) Ag NPs/α Ag$_2$WO$_4$-CE. (A, D) $t = 0$ s; (B and E) $t = 180$ s; (C, E) $t = 360$ s.
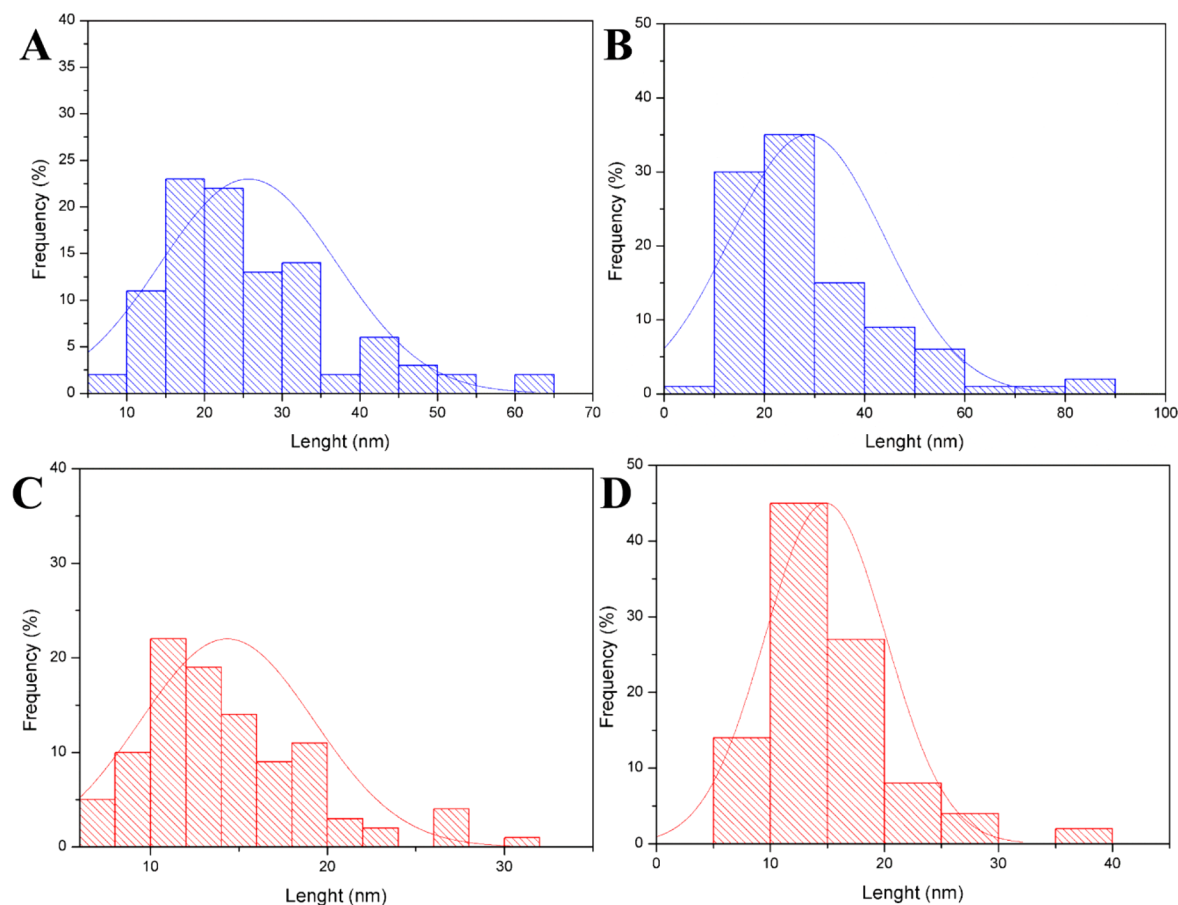
Figure 3. Average height and width distribution of Ag NPs on (A, B) Ag NPs/α-Ag$_2$WO$_4$-RE and (C, D) (Ag NPs/α-Ag$_2$WO$_4$-CE) composites, respectively, after electron irradiation via SEM.

of the excess electron density distribution must be caused by certain influential factors, such as the surface structure and morphology. According to our description, the possibility of formation of Ag NPs is the thermodynamic driving force of this process. Thus, as soon as the electron beam of the microscope hits the sample, the Ag NP growth process begins.[35,36,65] Figure 2 shows FE-SEM images of the two different morphologies (α-

Ag$_2$WO$_4$-R and α-Ag$_2$WO$_4$-C) after electron irradiation, resulting in Ag NPs/α-Ag$_2$WO$_4$-RE and Ag NPs/α-Ag$_2$WO$_4$-CE. Figure 2A,C shows the Ag NPs/α-Ag$_2$WO$_4$-RE at different times, $t = 0$, 180, and 360 s of electron beam exposure. Figure 2D,F shows the Ag NPs/α-Ag$_2$WO$_4$-CE at the same intervals. An analysis of the images reveals that, despite the fast initial Ag NP growth process, if we continuously irradiate the sample for a
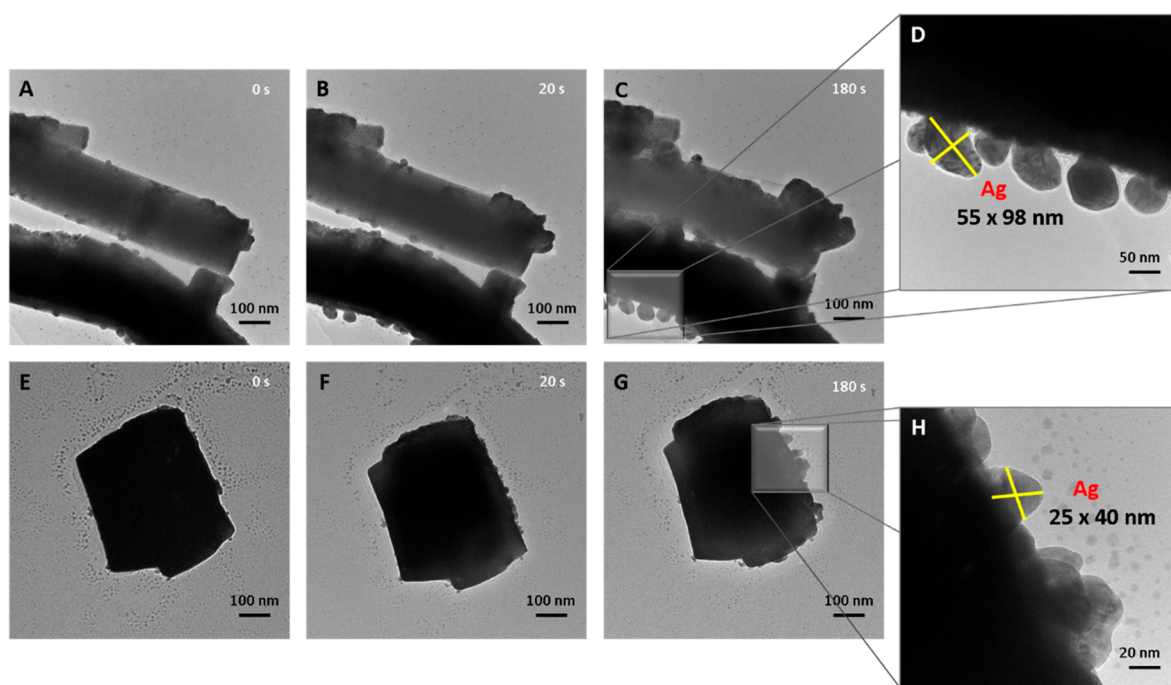
Figure 4. TEM images of Ag NPs/α-Ag$_2$WO$_4$ composites within a controlled time of exposure to a 200 kV electron beam. (A−D) Ag NPs/α-Ag$_2$WO$_4$-RE; (E−H) Ag NPs/α-Ag$_2$WO$_4$-CE samples. (A, E) t = 0 s; (B, F) t = 20 s; (C, G) t = 180 s; (D, H) higher magnifications of the nanoparticles after 180s.

longer period of time, we can observe certain similarities but also certain differences between the samples, Ag NPs/α-Ag$_2$WO$_4$-RE and Ag NPs/α-Ag$_2$WO$_4$-CE.

At t = 180s (see Figure 2B), it is possible to notice the presence of larger Ag NPs in Ag NPs/α-Ag$_2$WO$_4$-RE at the same positions with respect to Figure 2A (t = 0 s). If we continue irradiating the sample, we can notice an increase in the size of certain Ag NPs and the disappearance of certain others, until a point at which there is almost no change. From our observations, we infer that there is a stabilization of the Ag NP growth process after 300s of exposure. Figure 2C shows an image collected after a total period of 360 s, indicating the end of the Ag NP formation process. Figure 2D,F, for the Ag NPs/α-Ag$_2$WO$_4$-CE, reveal a similar behavior.

However, when we compare the NPs formed on each morphology, it is possible to sense that the formed Ag NPs are larger for the Ag NPs/α-Ag$_2$WO$_4$-RE than for the Ag NPs/Ag$_2$WO$_4$-CE composites, whereas in the latter there is a larger number of Ag NPs per unit area. Additionally, for both morphologies, there are certain facets that present regions with formation of Ag NPs, while other facets are completely smooth, which indicates a preferential Ag NP growth process. The red circles in Figure 2 emphasize the differences of certain Ag NPs within the duration of electron exposure, for the same sample and between the material morphologies.

In order to analyze the sizes of the Ag NPs, at least 100 Ag NPs on each electron-irradiated morphology were measured to build the corresponding histograms. Figure 3 displays the length distribution for the Ag NPs in two directions. From the data, we can see that the size of NPs on Ag NPs/α-Ag$_2$WO$_4$-RE shows a larger variation, from less than 10 to 90 nm, whereas the sizes of Ag NPs on Ag NPs/α-Ag$_2$WO$_4$-CE are in the range from less than 10 nm to 40 nm. The average values for the Ag NPs/α-Ag$_2$WO$_4$-RE morphology (26 ± 11 nm and 29 ± 15 nm) are

approximately twice the average dimensions of the Ag NPs on Ag NPs/Ag$_2$WO$_4$-CE (14 ± 5 nm and 15 ± 5 nm).

3.2. Ag Growth Process Induced by TEM. Owing to the higher electron energy and dosage, the Ag NP growth process is recognized to be faster and more intense for the TEM than for the SEM irradiation, and this should also affect the size of the Ag NPs. In fact, we know from previous studies with rod-like composites Ag NPs/α-Ag$_2$WO$_4$ that Ag NPs can become Ag filaments with an increased electron beam exposure.[35]

Figure 4 shows an analysis of the behavior of α-Ag$_2$WO$_4$-R and α-Ag$_2$WO$_4$-C samples inside a 200 kV TEM, at t = 0, 20, and 180 s, which yields Ag NPs/α-Ag$_2$WO$_4$-RE and Ag NPs/α-Ag$_2$WO$_4$-CE samples. We notice a clear increase in the size of the Ag NPs with an increased exposure time. However, after 180s, the Ag NPs stop increasing in size and attain the form observed in Figure 4D, which is a higher magnification of Figure 4C. Some of the particles in the inset (Figure 4D) reach approximately 100 nm in one dimension. In the case of Ag NPs/α-Ag$_2$WO$_4$-CE, there are several Ag NPs on one side of the cuboid morphology (Figure 4E,H), but they possess smaller sizes than those of the Ag NPs/Ag$_2$WO$_4$-RE sample. The larger Ag NPs observed at the higher magnification of Figure 4H for Ag NPs/Ag$_2$WO$_4$-CE are no larger than 25 × 40 nm^2, which is less than half in each dimension of the larger Ag NPs observed for the Ag NPs/Ag$_2$WO$_4$-RE (55 × 98 nm^2).

Furthermore, it is also possible to notice several smaller Ag NPs from the sample, deposited on the carbon film, which is more visible in the case of the Ag NPs/Ag$_2$WO$_4$-CE. This is the phenomenon of electron-beam-induced fragmentation (EBIF), which was already reported in the case of the irradiation of the rod-like morphology.[22,65] EBIF usually occurs when a micrometric target is exposed to an electron beam, with the increase in exposure time and current density, resulting in the fragmentation and ejection of NPs from the surface of the semiconductor. In a previous study reported by our group,[36] *ab initio*

calculations showed that the absorption of electrons leads to a disordered structure in α-Ag_2WO_4, which facilitates the nucleation of Ag NPs. Thus, we can infer that the level of disorder caused by the electron beam irradiation affects the Ag NP growth process. The higher number of Ag NPs observed on the carbon grid in the case of the Ag NPs/α-Ag_2WO_4-CE could be related to the effect of the beam when it interacts with this specific morphology.

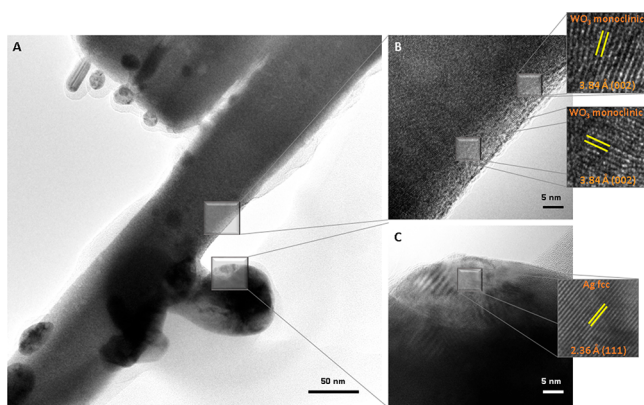Figure 5 presents HR-TEM images of Ag NPs located at the surface of the Ag NPs/α-Ag_2WO_4-RE sample after the electron

Figure 5. TEM analysis of the Ag NPs/α-Ag_2WO_4-RE sample after electron beam irradiation. (A) High-magnification TEM image of a single α-Ag_2WO_4 rod and Ag NPs. (B) HR-TEM image demonstrating the presence of small crystallites of WO_3 (insets) on the surface of the Ag_2WO_4-R. (C) HR-TEM image of a single Ag NP with an interplanar distance indexed to a cubic Ag NP (inset).

beam exposure by TEM, in order to gain a deeper insight into the structures formed during the electron beam irradiation. Figure 5B,C displays HR-TEM images of selected areas of Figure 5A to conduct the analysis. Some small crystallites are observed at the surface of the α-Ag_2WO_4-R (Figure 5B), where the crystallographic planes can be indexed to tungsten oxide, which is a better match with the most stable monoclinic structure according to the JCPDS database (PDF no. 43-1035). These findings are supported by the study of Merchan−Merchan et al.,[66] which demonstrated the stabilization of WO_x structures as an effect of TEM irradiation. In our case, the extraction of Ag from the α-Ag_2WO_4 lattice may lead to the formation of transitory $Ag_xW_yO_z$ nonstoichiometric domains at the surface of the initial semiconductor α-Ag_2WO_4-R[35,36,65] with the later stabilization of certain WO_3 nanodomains. However, it has a very limited extent and is undetectable by X-ray diffraction (XRD) because the region irradiated by electrons is very small and the semiconductor maintains its integrity, generating localized Ag vacancies and changing the properties of the material.

The distance between the crystallographic planes present in Ag NP was measured (Figure 5C) as 2.36 Å, which can be indexed to the interplanar distance of the (111) family of planes in metallic Ag with a face-centered cubic (fcc) structure, in accordance with the JCPDS database (PDF no. 04-0783). These (111) planes were also observed in the HR-TEM analysis of the Ag NPs/α-Ag_2WO_4-CE irradiated sample (Figure 6), demonstrating that both materials exhibit the formation of Ag with a typical fcc structure when irradiated with an electron beam. However, we are not able to observe a tungsten oxide structure on the surface of the Ag NPs/α-Ag_2WO_4-CE sample, probably
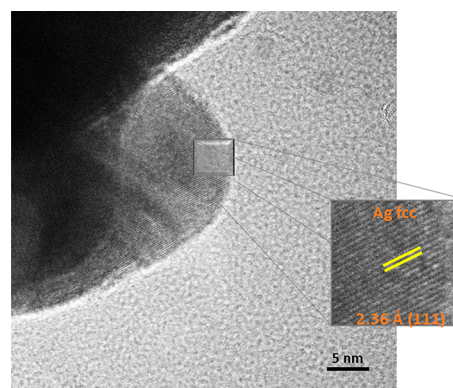

Figure 6. HR-TEM of a Ag NP on the Ag_2WO_4 surface of the Ag NPs/α-Ag_2WO_4-CE sample after TEM electron beam irradiation. Interplanar distances show the presence of the cubic fcc structure of Ag.

owing to the larger volumes of the cuboids in comparison to the rods, which hinder the TEM analysis in this particular case.

3.3. Ag Growth Process Induced by fs Laser Irradiation. The irradiation of solid materials with light, as with electron−matter interaction, is a quantum phenomenon. In the fs laser irradiation, photons are absorbed by α-Ag_2WO_4, inducing important modifications of the electron density cloud that affect the bond lengths and angles, leading to random and disordered structural changes that can result in a series of unexpected events.[40] During the fs laser irradiation, a plasma plume is generated, which is later deposited on the irradiated α-Ag_2WO_4 material. This plume is generally composed of several smaller metallic or nonstoichiometric oxides, depending on the process parameters.[40,57] If analyzed in isolation, the composition of the plume could be distinct from that of the remaining solid material. However, we solely analyzed the Ag NPs/α-Ag_2WO_4 composites, which are composed to a limited extent of the plume material.

Figures 7 and 8 show the STEM characterization in high-angle annular dark-field (HAADF) imaging mode and elemental mapping by EDS for the Ag NPs/α-Ag_2WO_4-RL and Ag NPs/α-Ag_2WO_4-CL samples, respectively. In both cases, it is possible to distinguish the regions where the Ag NPs are formed, leading to the formation of nonstoichiometric regions on the initial α-Ag_2WO_4 rods and cubes. More specifically, we conducted an EDS mapping of the Ag NPs/α-Ag_2WO_4-RL sample in the region shown in Figure 7B. The qualitative elemental distribution was performed using the Lα, Mα, and Kα lines for Ag (Figure 7C), W (Figure 7D), and O (Figure 7E), respectively. The region of the NPs formed on the initial α-Ag_2WO_4 rod shows an absolute predominance of Ag, which is also corroborated by the quantitative analysis by local EDS (region I). On the contrary, the EDS mapping of the region corresponding to the initial rod presents low-intensity Ag signals and also shows significant contributions of W and O. The quantitative analysis (region II) reflects these results, where major contributions of W and O are observed in comparison to Ag. These observations could be associated with the formation of nonstoichiometric regions and WO_3 nanodomains on the Ag NPs/Ag_2WO_4-RL sample.

A similar trend for the Ag NPs/α-Ag_2WO_4-CL sample is observed to that of the case of Ag NPs/α-Ag_2WO_4-RL sample. The analyzed region in this case contains several α-Ag_2WO_4 cuboids and Ag NPs (Figure 8B). The main Ag signal originates from the Ag NPs and to a lesser extent from the initial cuboids,
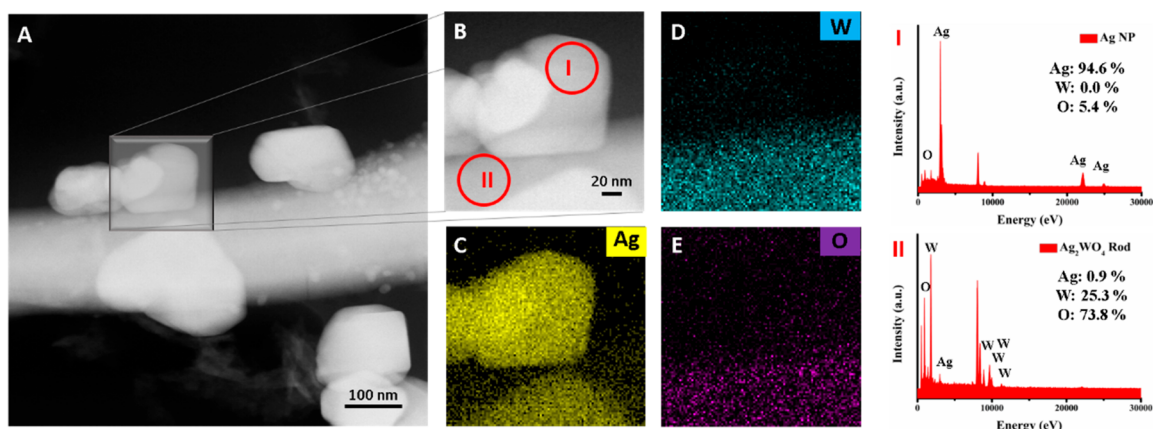
Figure 7. (A) TEM image of the Ag NPs/α-Ag$_2$WO$_4$-RL sample generated by the exposure to fs laser irradiation. (B–E) Energy-dispersive X-ray spectroscopy (EDS) mapping of the Ag NPs/α-Ag$_2$WO$_4$-RL sample. (I–II) Relative elementary quantification of the indicated areas in panel B.
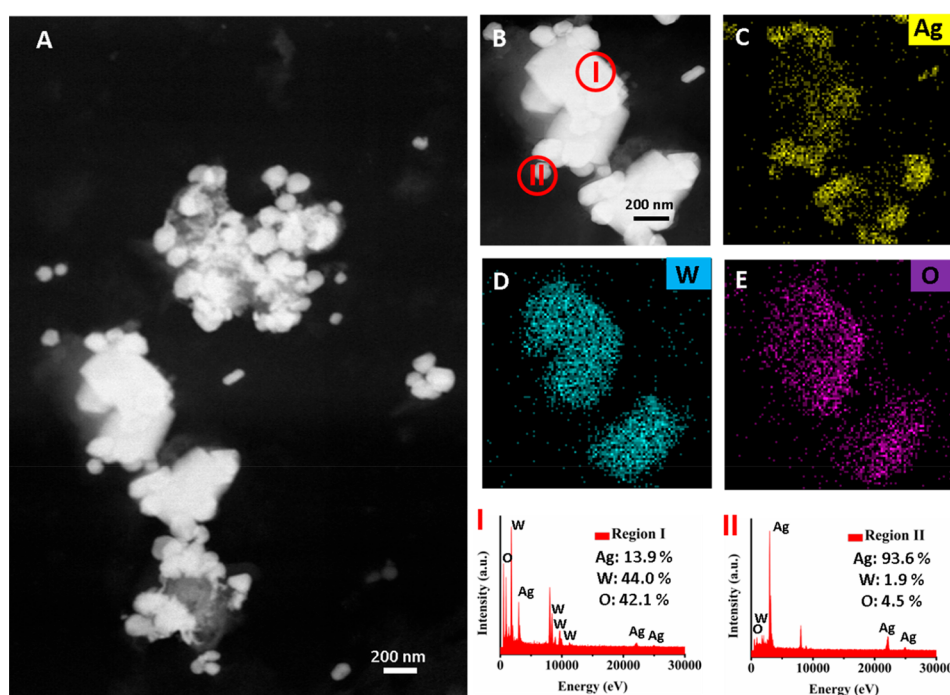

Figure 8. (A) TEM image of the Ag NPs/α-Ag$_2$WO$_4$-CL sample generated by the exposure to fs laser irradiation. (B–E) Energy-dispersive X-ray spectroscopy (EDS) mapping of the Ag NPs/α-Ag$_2$WO$_4$-CL sample. (I–II) Relative elementary quantification of the indicated areas in panel A.
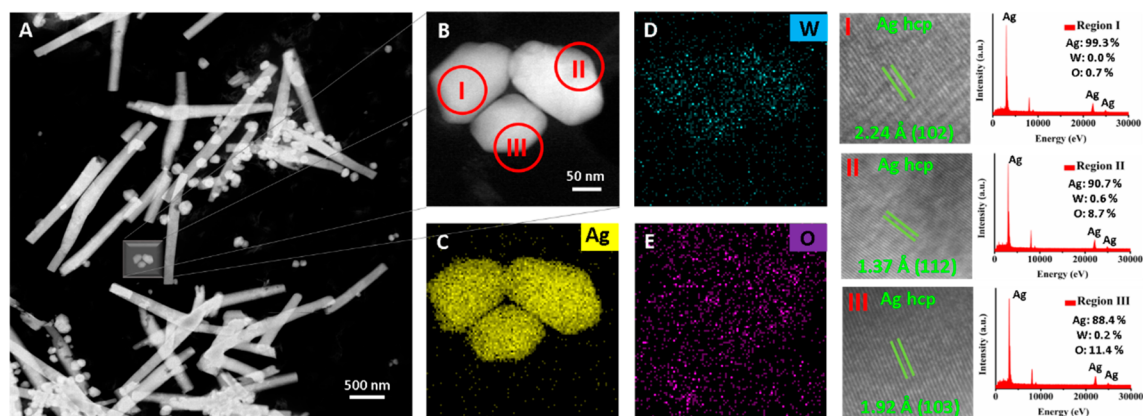

Figure 9. (A) HAADF image Ag NPs/α-Ag$_2$WO$_4$-RL. (B–E) EDS m. (I–III) HR-TEM of Ag NPs/α-Ag$_2$WO$_4$-RL and relative elemental quantifi cation of the indicated areas. The interplanar distances show the presence of Ag cubic and hexagonal structures.
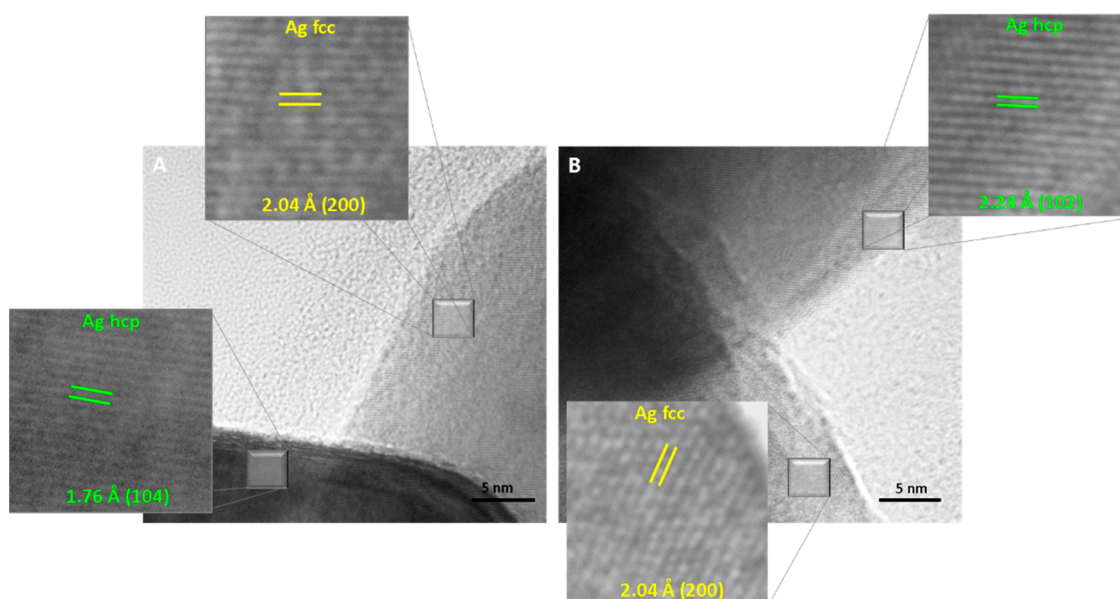
Figure 10. (A, B) HR-TEM of Ag NPs/α-Ag$_2$WO$_4$-CL. The interplanar distances show the presence of Ag cubic and hexagonal structures.
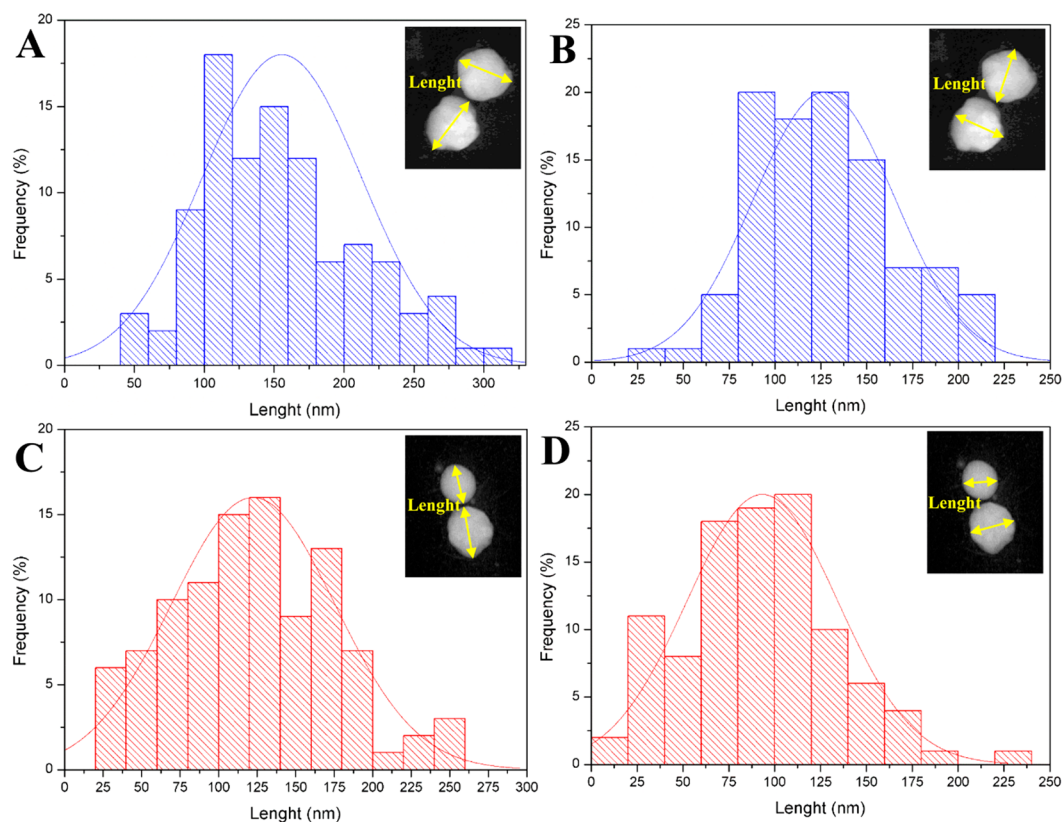

Figure 11. Average width and height distribution of Ag NPs on (A, B) Ag NPs/α-Ag$_2$WO$_4$-RL and (C, D) Ag NPs/α-Ag$_2$WO$_4$-CL after the irradiation by an fs laser.

jointly with the W and O signals (Figure 8D,E, respectively). The EDS quantification of regions corresponding to the initial cube (region I) and formed Ag NPs (region II) corroborates these findings.

Figures 9 and 10 show STEM and HR-TEM characterizations to gain a deeper understanding on the Ag structures generated on the Ag NPs/α-Ag$_2$WO$_4$-RL and Ag NPs/α-Ag$_2$WO$_4$-CL samples, respectively. For this analysis of the Ag NPs/Ag$_2$WO$_4$-

RL sample, we selected three isolated formed NPs (Figure 9A,B), which are mainly composed of Ag, as demonstrated by the EDS mappings (Figure 9C,D,E) as well by EDS local quantifications (regions I, II, and III). In these NPs, the distance between the crystallographic planes was measured, giving values of 2.24, 1.37, and 1.92 Å, which match well with the (102), (112), and (103) family of planes, respectively, of the unusual hexagonal polymorph (hcp) in accordance with the JCPDS

Table 1. All Superficial Metal Atoms (Ag and W) for Both (101) and (100) Surfaces with the Coordination Number (CN) and Oxidation Number (ON) for Initial (Optimized Geometries) and Final Configurations[a]

	(101) initial		(101) final		(100) initial			(100) final	
atom	CN	ON	CN	ON	atom	CN	ON	CN	ON
Ag-1	3	0.764	2	0.650	Ag-1	3	0.652	2	0.630
Ag-2	2	0.643	2	0.636	Ag-2	3	0652	2	0.644
Ag-3	3	0.700	3	0.694	Ag-3	4	0.719	3	0.600
Ag-4	2	0.657	2	0.607	Ag-4	4	0719	3	0.617
Ag-5	4	1.118	4	1.044	Ag-5	5	0673	2	0.528
W-1	5	2.579	5	2.555	Ag-6	5	0673	4	0.629
W-2	5	2.558	6	2.579	Ag-7	5	0.682	3	0.624
W-3	6	2.590	6	2.593	Ag-8	5	0.682	4	0.749
W-4	6	2.613	6	2.593	W-1	4	2.481	4	2.488
W-5	6	2.607	6	2.578	W-2	4	2.481	4	2.487
W-6	6	2.548	6	2.568	W-3	6	2.582	6	2.615
					W-4	6	2.582	6	2.556
A	159.99				146.17				
NA	112				84				

[a]From a 3 ps *ab initio* molecular simulation; surface area (A) in $Å^2$ and number of atoms (NA) in the computational supercell.

database (PDF no. 41-1402) related to the 4H phase. The regions analyzed in the Ag NPs/α-Ag$_2$WO$_4$-CL sample (insets in Figure 10A,B) demonstrated that both the fcc and hcp structures of Ag NPs could coexist when the samples were irradiated by an fs laser. Previous studies demonstrated that this polymorph could be naturally found in native silver distributed in ores as well as from synthetic sources.[67−69] Thus, an analysis of the results shows the formation of two polymorphs of metallic Ag, the common cubic structure, reported from the electron irradiation, and the metastable hexagonal structure, observed from the irradiation of α-Ag$_2$WO$_4$ material for the first time. We know from previous studies by our group that fs laser irradiation is capable of stabilizing metastable phases, as was reported by for Bi.[55]

Additionally, Figure 11 presents the size distribution in two dimensions, measured for at least 100 Ag NPs of each morphology. The sizes of the Ag NPs on the α-Ag NPs/Ag$_2$WO$_4$-RL sample range from 20 nm in one dimension to more than 300 nm in the other dimension, with an average width of 157 ± 57 nm and a height of 127 ± 39 nm, as can be observed in the histograms of Figure 11. We know from previous studies, that the fs laser irradiation usually promotes a wide range of sizes and shapes of NPs, as well as different crystallographic structures.[40,55] In Figures 8A and 9A, which are lower magnifications of the analyzed Ag NPs/Ag$_2$WO$_4$-RL and Ag NPs/Ag$_2$WO$_4$-CL samples, respectively, it is possible to observe several Ag NPs of different sizes and shapes, attached or not to the α-Ag$_2$WO$_4$. Assis et al.[55] pointed out the formation of spherical Ag NPs on α-Ag$_2$WO$_4$-R irradiated by an fs laser, whereas in this work we observe defined hexagons for the Ag NPs in the Ag NPs/α-Ag$_2$WO$_4$-CL and Ag NPs/α-Ag$_2$WO$_4$-RL samples.

3.5. Computational Results. As mentioned before, two morphologies are obtained: the cuboid morphology (α-Ag$_2$WO$_4$-C), which is composed of cubes and elongated cubes, in which the exposed surfaces are (010), (001), and (100), and the hexagonal, eight-facet rod-like morphology (α-Ag$_2$WO$_4$-R), with the surface composition of (010) and (001), but (101) instead of (100). The differences in composition are explained by the use of a surfactant agent that favors the crystal growth in one direction, stabilizing certain surfaces instead of others.[27] By the analysis of our present results, both of the

employed electron sources (SEM and TEM) were able to reduce the Ag$^+$ cation in the α-Ag$_2$WO$_4$ to form Ag NPs/α-Ag$_2$WO$_4$ composites, regardless of whether the material morphology involved (α-Ag$_2$WO$_4$-R or α-Ag$_2$WO$_4$-C). However, we can observe certain differences on the obtained Ag NPs for each morphology (size, distribution, etc.). In addition, we note that there seems to be a preferential facet growth. (Some facets are covered with several NPs and other facets are not.) The explanation for this lies in the differences in the surface compositions. At the top of each surface, there are different types of under-coordinated Ag and/or W cations with respect to the bulk. These local coordinations, associated with incomplete [AgO$_x$] and [WO$_y$] clusters, allow us to find the number of broken Ag−O and W−O bonds.

The local Ag NP growth process is dependent on two main subjects: the occurrence of Ag clusters and the presence of oxygen vacancies, which result in more positively charged Ag atoms. Although the (101) surface presents the larger value of E_{surf}, being the most energetic, its composition is formed mostly by WO$_6$ clusters, which compete for space with the under-coordinated silver clusters. The (010) surface, which appears in both systems, possess only one under-coordinated cluster of Ag, whereas the (001), which is also present in both systems, exhibits a combination of silver and under-coordinated tungstate clusters. The main difference is in the contrast between the (100) and (101) surfaces, where (100) presents a higher relative contribution of Ag clusters per surface area but smaller number of W clusters. In fact, as can be seen from Figure 12 and Table 1, the (100) surface exhibits eight Ag clusters, and four W clusters, whereas (101) only shows five Ag clusters but six W clusters. This indicates a higher density of superficial Ag atoms on the (100) surface than on the (101) surface.

We previously estimated the energy barrier for the most superficial Ag cations to diffuse outward in the (100) surface.[38,49] These barriers were calculated by using the nudged elastic band (NEB) method. In this approach, it is required to identify previously stable configurations, namely, final images, where diffusion processes would end. At this stage, there are different configurations in which a superficial Ag cation is displaced to an outward position followed by a geometrical optimization. However, it was found that only four of eight Ag cations are prone to diffuse, and the energy barrier of the process
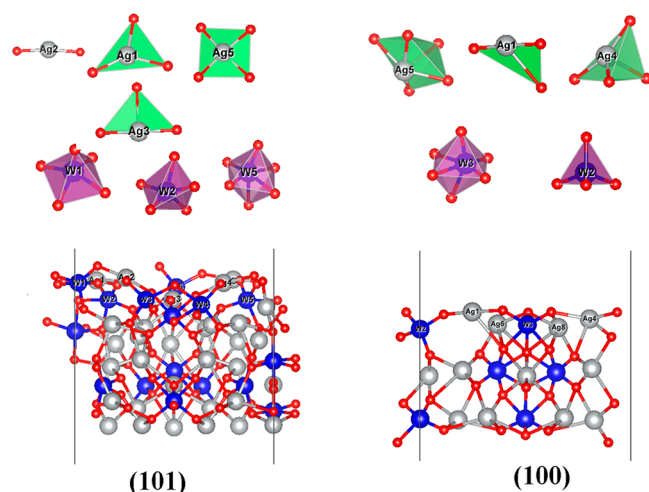
Figure 12. Lateral view (bottom) of the computational cells for (101) and (100) surfaces, and the cluster constituents (top). Ag, W, and O atoms are represented by gray, blue, and red balls, respectively.

is approximately 0.1 eV. In the process of finding the final images, the other four cations returned to their original positions. In this work, we investigated the (101) surface using this method and found that all of the superficial Ag cations are unable to initiate a diffusion process in a way similar to the (100) surface. In fact, it was observed that any trial for final images ends in different distorted clusters. This different structural behavior can also be confirmed from *ab initio* molecular dynamics simulations, which are supplied as Supporting Information. From Videos S1 and S2, it can be seen that simulations at room temperature show, despite the typical thermal fluctuations, a few observed effects on the (101) surface, which mostly retains the initial arrangement through the simulation. Conversely, the (100) termination changes significantly, and the initial superficial Ag clusters are altered to new geometrical arrangements, whose coordination numbers also change as reported in Table 1. Interestingly, these structural changes leave the Ag atoms more exposed with smaller coordination numbers, in agreement with the previous NEB calculations.

The differences between the electronic environments in both morphologies were studied by comparing the electron density distributions using the QTAIM. A quantitative comparative analysis was done from the oxidation numbers (ON), which were computed as the difference between the number of valence electrons and the Bader charge (q_M). Table 1 reports the oxidation numbers (ON) for each superficial metal atom. Thus, for the initial configurations, the mean ONs for Ag are +0.776 and +0.682 in the (101) and (100) surfaces, respectively. Additionally, for the other configurations found in the *ab initio* molecular simulations, the Ag atoms are always more reduced in the (100) surface. Furthermore, this surface shows a higher number of superficial Ag atoms with similar oxidation states, when compared to the (101) surface, where Ag atoms have different oxidation states. This evidence might be favorable in the (100) surface for a more effective surface−electron-beam interaction, and a rapid and intense Ag nucleation could be expected. In addition, as has been reported in previous computational studies, this surface is the most energetically favored to undergo the diffusion process to grow metallic Ag.[38] These facts agree with the observed details in the cubic

morphology (many Ag NPs of smaller dimensions). We consider that this may be related specifically to the (100) facet.

In the case of the fs laser irradiation, it is more difficult to discern a relation between the facets and the Ag growth process, because most Ag NPs are already out of the surface of the semiconductor material (see Figures 7A and 8A). However, the sample is much more uniformly reached by the laser than in the case of the electrons, and in this case, the symmetry of the morphology could be more important, so the α-Ag$_2$WO$_4$-C can be the favored candidate to generate more Ag NPs.

3.4. Antimicrobial Activity. The values for the minimum bactericidal concentration (MBC) against MRSA are presented in Table 2. The results show that α-Ag$_2$WO$_4$-R is twice as

Table 2. Minimum Bactericidal Concentration (MBC) for the α-Ag2WO$_4$ Samples against MRSA

sample	minimal bactericidal concentration (μg/mL)
α-Ag$_2$WO$_4$-R	128
α-Ag$_2$WO$_4$-C	256
α-Ag$_2$WO$_4$-RE	32
α-Ag$_2$WO$_4$-CE	128
α-Ag$_2$WO$_4$-RL	8
α-Ag$_2$WO$_4$-CL	4

effective as the α-Ag$_2$WO$_4$-C. However, as expected from previous studies, the electron irradiation is able to increase the bactericide effect, such that the Ag NPs/α-Ag$_2$WO$_4$-RE is four times more efficient than the nonirradiated sample, and the Ag NPs/α-Ag$_2$WO$_4$-CE is twice as efficient as the original nonirradiated sample. The enhancement induced by the laser irradiation is even more impressive. Compared to the non-irradiated α-Ag$_2$WO$_4$-R, the laser-irradiated sample, Ag NPs/α-Ag$_2$WO$_4$-RL, is 16 times more potent to kill the tested microbe, and the Ag NPs/α-Ag$_2$WO$_4$-CL is, incredibly, 64 times more effective to kill the microbe, which is twice as effective as the laser-irradiated Ag NPs/α-Ag$_2$WO$_4$-RL. To summarize, in general, the rod-like morphology has a higher antimicrobial activity, except when laser-irradiated, which enables the cuboid morphology to become the most powerful agent.

Several studies have reported the antimicrobial activity of rod-like α-Ag$_2$WO$_4$-R against Gram-positive and Gram-negative bacteria, as well as fungi.[33,34] In addition to being effective against several microorganisms, it is not cytotoxic to certain human cell lines, which makes it a promising material for many biological applications. The antimicrobial activity of α-Ag$_2$WO$_4$ is intrinsically related to the morphology, size, and structural alterations caused by external agents. Longo et al.[32] synthesized α-Ag$_2$WO$_4$ by a microwave-assisted hydrothermal method and irradiated a sample with electrons for 30 min under a FE-SEM. The samples were tested against MRSA, and a 4-fold improvement in the effectiveness was observed for the sample that was irradiated with electrons. The same was observed when rod-like α-Ag$_2$WO$_4$-R was irradiated by an fs laser, where the fs-laser-irradiated composite (Ag NPs/α-Ag$_2$WO$_4$-RL) was 32 times more effective than the nonirradiated sample.[40] The similarity between the studies is the structural modification in α-Ag$_2$WO$_4$ through irradiation, leading to the nucleation of metallic Ag NPs on the surface of the materials, thus increasing their antibacterial activity. Our results for the Ag NPs/α-Ag$_2$WO$_4$-RE irradiated with electrons under the same conditions (30 min in a 30-keV FE-SEM) are very similar to those in the literature, showing a 4-fold increase in the

antibacterial activity. In the case of the fs laser irradiation, the results are also coherent, once we used the α-Ag$_2$WO$_4$-R irradiated material and not only the plume (smaller Ag NPs), as was the case of the mentioned work.[40]

In the case of the cuboid samples, α-Ag$_2$WO$_4$-C, they were less active against the tested microorganism. Apart from being the theoretical ideal morphology of α-Ag$_2$WO$_4$, it proved highly inactive for other tested properties, such as photocatalysis.[27] Despite the differences in mechanisms between these properties (photocatalysis and bactericide activity), it proved to be less reactive than the α-Ag$_2$WO$_4$-R morphology. Although the α-Ag$_2$WO$_4$-C showed less reactivity, the electron irradiation doubled its activity, making it comparable to the pure rod-like morphology, α-Ag$_2$WO$_4$-R. Furthermore, the fs-laser-irradiated sample showed an amazing improvement in relation to the pure sample, where the Ag NPs/α-Ag$_2$WO$_4$-CL composite was almost 64 times more powerful, and was the sample with the highest antimicrobial activity of all of the tested samples.

As stated before, it is difficult to compare the results of the electron and fs laser irradiations. The electron beam of the microscope possesses a much lower penetrating power and is probably not able to sweep the whole sample. In this case, the characteristics of the surface play an important role, and we can observe a preferential Ag NP growth process. However, the fs laser has a much greater penetrating power and is capable of generating a higher number of Ag NPs of several sizes and shapes, which are in most cases not adhered to the surface and free to react.

Furthermore, the size of the Ag NPs also directly influences the antibacterial activity, as well as the concentration.[34] The cuboid samples, in addition to being smaller in size, also present more Ag NPs on the surface, which are also smaller in relation to the surface Ag NPs of the irradiated rod-like morphology, α-Ag$_2$WO$_4$-R. The improvement in the antibacterial activity can be attributed to the increase in the surface area/volume ratio of the surface, with the decrease in the particle size. As the size of the surface Ag NPs decreases, the surface area/volume proportion for individual particles increases and the relative concentration of particles also increases, thus increasing the overall ratio of Ag NPs in the system.[70] Additionally, the fs-laser-irradiated samples are composed not only by the common and more stable cubic crystallographic structure but also by the metastable hexagonal structure, which is another important factor for the reactivity improvement.

4. CONCLUSIONS

We studied the Ag NP growth process on two morphologies of α-Ag$_2$WO$_4$: a hexagonal, eight-facet elongated rod-like (α-Ag$_2$WO$_4$-R) structure and a cuboid one (α-Ag$_2$WO$_4$-C), irradiated by electron beams of SEM and TEM, as well as an fs laser. The nonirradiated samples, α-Ag$_2$WO$_4$-R and α-Ag$_2$WO$_4$-C, and the irradiated Ag NPs/α-Ag$_2$WO$_4$ composites (SEM and fs laser) were evaluated with respect to their bactericidal activity against MRSA. The variations in surface morphology, chemical composition, and crystallinity of the resulting Ag NPs were observed by FE-SEM, *in situ* TEM, HR-TEM, and EDS compositional analysis. In addition, to complement the experimental results, first-principles calculations have been performed. The integration of experimental results and computational modeling can undoubtedly lead to a new level of insight.

The main conclusions can be summarized as follows: (i) For both electron and fs laser irradiations, the morphology plays an

important role and can direct the growth of Ag NPs. In the case of the fs laser irradiation, a large number of Ag NPs can be sensed for the Ag NPs/α-Ag$_2$WO$_4$-C samples. (ii) First-principles calculations allow us to associate the presence of the (100) surface, in which the Ag cations might initiate an earlier diffusion process to yield a higher ratio of Ag NPs per surface area in the α-Ag$_2$WO$_4$-C samples. (iii) Conversely, simulations show that in the (101) surface, which is exhibited in the α-Ag$_2$WO$_4$-R samples, the superficial Ag cations should follow different diffusive mechanisms, leading to fewer and larger Ag NPs than for the α-Ag$_2$WO$_4$-C samples; (iv) α-Ag$_2$WO$_4$-R material proved to be a better bactericidal agent, against MRSA, for most cases, except for the fs-laser-irradiated Ag NPs/α-Ag$_2$WO$_4$-CL sample. (v) A drastic bacterial enhancement was observed for the Ag NPs/α-Ag$_2$WO$_4$-CL sample irradiated by an fs laser. (vi) The ultrashort pulses of an fs laser are even able to promote the stabilization of metastable phases that only are possible under extreme conditions. We observed, for the first time, the appearance of the hexagonal structure of metallic Ag NPs under these conditions. (vii) Furthermore, these Ag NPs/α-Ag$_2$WO$_4$ composites presented, in general, a high bactericidal activity and high thermal stability, which is very encouraging for future applications, as well as for the extension of the method to other composites. (viii) Hence, we foresee that the spatiotemporal control of nucleation and crystal growth by an fs laser will provide a new approach toward obtaining functional crystals that have not been achieved by conventional methods. These results on the synthesis and stability of Ag NPs/α-Ag$_2$WO$_4$ composites provide a potential extension of the methods to produce materials with catalytic applications. (ix) While it is clear that computational modeling can play a significant role in facilitating enhanced interpretation and understanding of experimental observations, the next step to be taken is the computational design of the next generation of innovative materials as bactericides or even catalysts. Theoretical advances make the *in silico* design of new catalysts with tailored properties an increasingly realistic prospect. It is increasingly likely that the integration of computational design and experiments in a feedback loop may provide such a step change. The general methodology and insights gained from our study strengthen our understanding of synthesis control because the structural and bactericidal activities are encoded in the exposed surfaces, i.e., the morphology of the α-Ag$_2$WO$_4$ material.

■ ASSOCIATED CONTENT

Ⓢ Supporting Information

The Supporting Information is available free of charge on the ACS Publications website at DOI: 10.1021/acsabm.8b00673.

Video descriptions (PDF)

Video S1 (MPG)

Video S2 (MPG)

■ AUTHOR INFORMATION

ORCID Ⓞ

Nadia G. Macedo: 0000-0001-7031-2729

Thales R. Machado: 0000-0002-3246-6329

Roman A. Roca: 0000-0002-2938-412X

Marcelo Assis: 0000-0003-0355-5565

Camila Cristina Foggi: 0000-0002-1210-1234

Verónica Puerto-Belda: 0000-0001-7030-2977

Gladys Mínguez-Vega: 0000-0003-4994-1859

André Rodrigues: 0000-0002-4086-7704
Miguel A. San-Miguel: 0000-0002-6650-7432
Héctor Beltrán-Mir: 0000-0002-7836-1602
Juan Andrés: 0000-0003-0232-3957
Elson Longo: 0000-0001-8062-7791

Notes
The authors declare no competing financial interest.

■ ACKNOWLEDGMENTS

■ REFERENCES

(1) Peng, Y.-K.; Tsang, S. C. E. Facet-Dependent Photocatalysis of Nanosize Semiconductive Metal Oxides and Progress of Their Characterization. *Nano Today* **2018**, *18*, 15−34.

(2) Liu, G.; Yu, J. C.; Lu, G. Q.; Cheng, H.-M. Crystal Facet Engineering of Semiconductor Photocatalysts: Motivations, Advances and Unique Properties. *Chem. Commun.* **2011**, *47*, 6763−6783.

(3) Lapworth, D. J.; Baran, N.; Stuart, M. E.; Ward, R. S. Emerging Organic Contaminants in Groundwater: A Review of Sources, Fate and Occurrence. *Environ. Pollut.* **2012**, *163*, 287−303.

(4) Mouele, E. S.; Tijani, J. O.; Fatoba, O. O.; Petrik, L. F. Degradation of Organic Pollutants and Microorganisms from Wastewater Using Different Dielectric Barrier Discharge Configurations: A Critical Review. *Environ. Sci. Pollut. Res.* **2015**, *22*, 18345−18362.

(5) Fresno, F.; Portela, R.; Suárez, S.; Coronado, J. M. Photocatalytic Materials: Recent Achievements and Near Future Trends. *J. Mater. Chem. A* **2014**, *2*, 2863−2884.

(6) Henderson, M. A. A Surface Science Perspective on TiO$_2$ Photocatalysis. *Surf. Sci. Rep.* **2011**, *66*, 185−297.

(7) Wang, H.; Zhang, L.; Chen, Z.; Hu, J.; Li, S.; Wang, Z.; Liu, J.; Wang, X. Semiconductor Heterojunction Photocatalysts: Design, Construction, and Photocatalytic Performances. *Chem. Soc. Rev.* **2014**, *43*, 5234−5244.

(8) Kochuveedu, S. T.; Jang, Y. H.; Kim, D. H. A Study on the Mechanism for the Interaction of Light with Noble Metal-Metal Oxide Semiconductor Nanostructures for Various Photophysical Applications. *Chem. Soc. Rev.* **2013**, *42*, 8467−8493.

(9) Sim, L. C.; Leong, K. H.; Ibrahim, S.; Saravanan, P. Graphene Oxide and Ag Engulfed TiO$_2$ Nanotube Arrays for Enhanced Electron Mobility and Visible-Light-Driven Photocatalytic Performance. *J. Mater. Chem. A* **2014**, *2*, 5315−5322.

(10) Liu, H.; Hu, C.; Zhai, H.; Yang, J.; Liu, X.; Jia, H. Fabrication of In2O3/ZnO@Ag Nanowire Ternary Composites with Enhanced Visible Light Photocatalytic Activity. *RSC Adv.* **2017**, *7*, 37220−37229.

(11) Rizzello, L.; Pompa, P. P. Nanosilver-Based Antibacterial Drugs and Devices: Mechanisms, Methodological Drawbacks, and Guidelines. *Chem. Soc. Rev.* **2014**, *43*, 1501−1518.

(12) Chernousova, S.; Epple, M. Silver as Antibacterial Agent: Ion, Nanoparticle, and Metal. *Angew. Chem., Int. Ed.* **2013**, *52*, 1636−1653.

(13) Linic, S.; Christopher, P.; Ingram, D. B. Plasmonic-Metal Nanostructures for Efficient Conversion of Solar to Chemical Energy. *Nat. Mater.* **2011**, *10*, 911−921.

(14) Rycenga, M.; Cobley, C. M.; Zeng, J.; Li, W.; Moran, C. H.; Zhang, Q.; Qin, D.; Xia, Y. Controlling the Synthesis and Assembly of Silver Nanostructures for Plasmonic Applications. *Chem. Rev.* **2011**, *111*, 3669−3712.

(15) Wang, L.; Yu, M.; Wu, C.; Deng, N.; Wang, C.; Yao, X. Synthesis of Ag/g-C$_3$N$_4$ Composite as Highly Efficient Visible-Light Photocatalyst for Oxidative Amidation of Aromatic Aldehydes. *Adv. Synth. Catal.* **2016**, *358*, 2631−2641.

(16) Zhao, W.; Guo, Y.; Faiz, Y.; Yuan, W.-T.; Sun, C.; Wang, S.-M.; Deng, Y.-H.; Zhuang, Y.; Li, Y.; Wang, X.-M.; He, H.; Yang, S.-G. Facile in-Suit Synthesis of Ag/AgVO$_3$ One-Dimensional Hybrid Nanoribbons with Enhanced Performance of Plasmonic Visible-Light Photocatalysis. *Appl. Catal., B* **2015**, *163*, 288−297.

(17) Tobaldi, D. M.; Piccirillo, C.; Pullar, R. C.; Gualtieri, A. F.; Seabra, M. P.; Castro, P. M. L.; Labrincha, J. A. Silver-Modified Nano-Titania as an Antibacterial Agent and Photocatalyst. *J. Phys. Chem. C* **2014**, *118*, 4751−4766.

(18) Kuriakose, S.; Choudhary, V.; Satpati, B.; Mohapatra, S. Facile Synthesis of Ag-ZnO Hybrid Nanospindles for Highly Efficient Photocatalytic Degradation of Methyl Orange. *Phys. Chem. Chem. Phys.* **2014**, *16*, 17560−17568.

(19) Jaramillo-Páez, C.; Navío, J. A.; Hidalgo, M. C.; Macías, M. High UV- Photocatalytic Activity of ZnO and Ag/ZnO Synthesized by a Facile Method. *Catal. Today* **2017**, *284*, 121−128.

(20) Li, J.; Liu, F.; Li, Y. Fabrication of an Ag/Ag$_2$MoO$_4$ Plasmonic Photocatalyst with Enhanced Photocatalytic Performance for the Degradation of Ciprofloxacin. *New J. Chem.* **2018**, *42*, 12054−12061.

(21) Lee, H.; Lee, Y. K.; Hwang, E.; Park, J. Y. Enhanced Surface Plasmon Effect of Ag/TiO$_2$ Nanodiodes on Internal Photoemission. *J. Phys. Chem. C* **2014**, *118*, 5650−5656.

(22) Gonzalez-Martinez, I. G.; Bachmatiuk, A.; Bezugly, V.; Kunstmann, J.; Gemming, T.; Liu, Z.; Cuniberti, G.; Rümmeli, M. H. Electron-Beam Induced Synthesis of Nanostructures: A Review. *Nanoscale* **2016**, *8*, 11340−11362.

(23) Xiong, W.; Zhou, Y.; Hou, W.; Jiang, L.; Mahjouri-Samani, M.; Park, J.; He, X.; Gao, Y.; Fan, L.; Baldacchini, T.; Silvain, J.-F.; Lu, Y. Laser-Based Micro/Nanofabrication in One, Two and Three dimensions. *Front. Opt.* **2015**, *8*, 351−378.

(24) Cavalcante, L. S.; Almeida, M. A. P.; Avansi, W.; Tranquilin, R. L.; Longo, E.; Batista, N. C.; Mastelaro, V. R.; Li, M. S. Cluster Coordination and Photoluminescence Properties of α-Ag$_2$WO$_4$Microcrystals. *Inorg. Chem.* **2012**, *51*, 10675−10687.

(25) De Santana, Y. V. B.; Gomes, J. E. C.; Matos, L.; Cruvinel, G. H.; Perrin, A.; Perrin, C.; Andrés, J.; Varela, J. A.; Longo, E. Silver Molybdate and Silver Tungstate Nanocomposites with Enhanced Photoluminescence. *Nanomater. Nanotechnol.* **2014**, *4*, 22.

(26) Roca, R. A.; Sczancoski, J. C.; Nogueira, I. C.; Fabbro, M. T.; Alves, H. C.; Gracia, L.; Santos, L. P. S.; de Sousa, C. P.; Andrés, J.; Luz, G. E.; Longo, E.; Cavalcante, L. S. Facet-Dependent Photocatalytic and Antibacterial Properties of α-Ag$_2$WO$_4$Crystals: Combining Experimental Data and Theoretical Insights. *Catal. Sci. Technol.* **2015**, *5*, 4091−4107.

(27) Macedo, N. G.; Gouveia, A. F.; Roca, R. A.; Assis, M.; Gracia, L.; Andrés, J.; Leite, E. R.; Longo, E. Surfactant-Mediated Morphology and Photocatalytic Activity of α-Ag₂WO₄ Material. *J. Phys. Chem. C* **2018**, *122*, 8667−8679.

(28) Lin, Z.; Li, J.; Zheng, Z.; Yan, J.; Liu, P.; Wang, C.; Yang, G. W. Electronic Reconstruction of Ag₂WO₄ Nanorods for the Visible-Light Photocataysis. *ACS Nano* **2015**, *9*, 7256−7265.

(29) da Silva, L. F.; Catto, A. C.; Avansi, W., Jr.; Cavalcante, L. S.; Andres, J.; Aguir, K.; Mastelaro, V. R.; Longo, E. A Novel Ozone Gas Sensor Based on One-Dimensional (1D) Alpha-Ag₂WO₄ Nanostructures. *Nanoscale* **2014**, *6*, 4058−4062.

(30) Sreedevi, A.; Priyanka, K. P.; Vattappalam, S. C.; Varghese, T. Silver Tungstate Nanoparticles for the Detection of Ethanol, Ammonia and Acetone Gases. *J. Electron. Mater.* **2018**, *47*, 6328−6333.

(31) da Silva, L. F.; Catto, A. C.; Avansi, W.; Cavalcante, L. S.; Mastelaro, V. R.; Andrés, J.; Aguir, K.; Longo, E. Acetone Gas Sensor Based on α-Ag₂WO₄ Nanorods Obtained Via a Microwave-Assisted Hydrothermal Route. *J. Alloys Compd.* **2016**, *683*, 186−190.

(32) Longo, V. M.; De Foggi, C. C.; Ferrer, M. M.; Gouveia, A. F.; Andre, R. S.; Avansi, W.; Vergani, C. E.; Machado, A. L.; Andres, J.; Cavalcante, L. S.; Hernandes, A. C.; Longo, E. Potentiated Electron Transference in Alpha-Ag₂WO₄ Microcrystals with Ag Nanofilaments as Microbial Agent. *J. Phys. Chem. A* **2014**, *118*, 5769−5778.

(33) de Foggi, C. C.; de Oliveira, R. C.; Fabbro, M. T.; Vergani, C. E.; Andres, J.; Longo, E.; Machado, A. L. Tuning the Morphological, Optical, and Antimicrobial Properties of α-Ag₂WO₄ Microcrystals Using Different Solvents. *Cryst. Growth Des.* **2017**, *17*, 6239−6246.

(34) Foggi, C. C.; Fabbro, M. T.; Santos, L. P. S.; de Santana, Y. V. B.; Vergani, C. E.; Machado, A. L.; Cordoncillo, E.; Andrés, J.; Longo, E. Synthesis and Evaluation of α-Ag₂WO₄ as Novel Antifungal Agent. *Chem. Phys. Lett.* **2017**, *674*, 125−129.

(35) Longo, E.; Cavalcante, L. S.; Volanti, D. P.; Gouveia, A. F.; Longo, V. M.; Varela, J. A.; Orlandi, M. O.; Andres, J. Direct in Situ Observation of the Electron-Driven Synthesis of Ag Filaments on Alpha-Ag₂WO₄ Crystals. *Sci. Rep.* **2013**, *3*, 1676.

(36) Longo, E.; Volanti, D. P.; Longo, V. M.; Gracia, L.; Nogueira, I. C.; Almeida, M. A. P.; Pinheiro, A. N.; Ferrer, M. M.; Cavalcante, L. S.; Andrés, J. Toward an Understanding of the Growth of Ag Filaments on α-Ag₂WO₄ and their Photoluminescent Properties: A Combined Experimental and Theoretical Study. *J. Phys. Chem. C* **2014**, *118*, 1229−1239.

(37) Andrés, J.; Gracia, L.; Gonzalez-Navarrete, P.; Longo, V. M.; Avansi, W., Jr.; Volanti, D. P.; Ferrer, M. M.; Lemos, P. S.; La Porta, F. A.; Hernandes, A. C.; Longo, E. Structural and Electronic Analysis of the Atomic Scale Nucleation of Ag on Alpha-Ag₂WO₄ Induced by Electron Irradiation. *Sci. Rep.* **2015**, *4*, 5391.

(38) Pereira, W. d. S.; Andrés, J.; Gracia, L.; San-Miguel, M. A.; da Silva, E. Z.; Longo, E.; Longo, V. M. Elucidating the Real-Time Ag Nanoparticle Growth on α-Ag₂WO₄ During Electron Beam Irradiation: Experimental Evidence and Theoretical Insights. *Phys. Chem. Chem. Phys.* **2015**, *17*, 5352−5359.

(39) San-Miguel, M. A.; da Silva, E. Z.; Zanetti, S. M.; Cilense, M.; Fabbro, M. T.; Gracia, L.; Andres, J.; Longo, E. In Situ Growth of Ag Nanoparticles on Alpha-Ag₂WO₄ under Electron Irradiation: Probing the Physical Principles. *Nanotechnology* **2016**, *27*, 225703.

(40) Assis, M.; Cordoncillo, E.; Torres-Mendieta, R.; Beltran-Mir, H.; Minguez-Vega, G.; Oliveira, R.; Leite, E. R.; Foggi, C. C.; Vergani, C. E.; Longo, E.; Andres, J. Towards the Scale-up of the Formation of Nanoparticles on Alpha-Ag₂WO₄ with Bactericidal Properties by Femtosecond Laser Irradiation. *Sci. Rep.* **2018**, *8*, 1884.

(41) Roca, R. A.; Gouveia, A. F.; Lemos, P. S.; Gracia, L.; Andrés, J.; Longo, E. Formation of Ag Nanoparticles on β-Ag₂WO₄ through Electron Beam Irradiation: A Synergetic Computational and Experimental Study. *Inorg. Chem.* **2016**, *55*, 8661−8671.

(42) Alvarez Roca, R.; Lemos, P. S.; Andrés, J.; Longo, E. Formation of Ag Nanoparticles on Metastable β-Ag₂WO₄ Microcrystals Induced by Electron Irradiation. *Chem. Phys. Lett.* **2016**, *644*, 68−72.

(43) Fabbro, M. T.; Saliby, C.; Rios, L. R.; La Porta, F. A.; Gracia, L.; Li, M. S.; Andrés, J.; Santos, L. P.; Longo, E. Identifying and Rationalizing the Morphological, Structural, and Optical Properties of β-Ag₂MoO₄ Microcrystals, and the Formation Process of Ag Nanoparticles on their Surfaces: Combining Experimental Data and First-Principles Calculations. *Sci. Technol. Adv. Mater.* **2015**, *16*, 065002.

(44) Andrés, J.; Ferrer, M. M.; Gracia, L.; Beltran, A.; Longo, V. M.; Cruvinel, G. H.; Tranquilin, R. L.; Longo, E. A Combined Experimental and Theoretical Study on the Formation of Ag Filaments on β-Ag₂MoO₄ Induced by Electron Irradiation. *Part. Part. Syst. Char.* **2015**, *32*, 646−651.

(45) Fabbro, M. T.; Gracia, L.; Silva, G. S.; Santos, L. P. S.; Andrés, J.; Cordoncillo, E.; Longo, E. Understanding the Formation and Growth of Ag Nanoparticles on Silver Chromate Induced by Electron Irradiation in Electron Microscope: A Combined Experimental and Theoretical Study. *J. Solid State Chem.* **2016**, *239*, 220−227.

(46) de Oliveira, R. C.; Assis, M.; Teixeira, M. M.; da Silva, M. D. P.; Li, M. S.; Andres, J.; Gracia, L.; Longo, E. An Experimental and computational study of β-AgVO₃ Optical properties and formation of Ag Nanoparticles. *J. Phys. Chem. C* **2016**, *120*, 12254−12264.

(47) Botelho, G.; Sczancoski, J. C.; Andres, J.; Gracia, L.; Longo, E. Experimental and Theoretical Study on the Structure, Optical Properties, and Growth of Metallic Silver Nanostructures in Ag₃PO₄. *J. Phys. Chem. C* **2015**, *119*, 6293−6306.

(48) Andrés, J.; Longo, E.; Gouveia, A. F.; Costa, J. P.C.; Gracia, L.; Oliveira, M. C. *In Situ* Formation of Metal Nanoparticles Through Electron Beam Irradiation: Modeling Real Materials from First-Principles Calculations. *J. Mater. Sci. Eng.* **2018**, *7*, 461.

(49) Andrés, J.; Gouveia, A. F.; Gracia, L.; Longo, E.; Manzeppi Faccin, G.; da Silva, E. Z.; Pereira, D. H.; San-Miguel, M. A. Formation of Ag Nanoparticles under Electron Beam Irradiation: Atomistic Origins from First-Principles Calculations. *Int. J. Quantum Chem.* **2018**, *118*, No. e25551.

(50) Faccin, G. M.; San-Miguel, M. A.; Andres, J.; Longo, E.; da Silva, E. Z. Computational Modeling for the Ag Nanoparticle Coalescence Process: A Case of Surface Plasmon Resonance. *J. Phys. Chem. C* **2017**, *121*, 7030−7036.

(51) Zhou, X.; Liu, G.; Yu, J.; Fan, W. Surface Plasmon Resonance-Mediated Photocatalysis by Noble Metal-Based Composites under Visible Light. *J. Mater. Chem.* **2012**, *22*, 21337−21354.

(52) Wang, P.; Huang, B.; Dai, Y.; Whangbo, M. H. Plasmonic Photocatalysts: Harvesting Visible Light with Noble Metal Nanoparticles. *Phys. Chem. Chem. Phys.* **2012**, *14*, 9813−9825.

(53) Ma, H. L.; Yang, J. Y.; Dai, Y.; Zhang, Y. B.; Lu, B.; Ma, G. H. Raman Study of Phase Transformation of TiO₂ Rutile Single Crystal Irradiated by Infrared Femtosecond Laser. *Appl. Surf. Sci.* **2007**, *253*, 7497−7500.

(54) Yan, P. F.; Du, K.; Sui, M. L. α- to γ-Al₂O₃ Martensitic Transformation Induced by Pulsed Laser Irradiation. *Acta Mater.* **2010**, *58*, 3867−3876.

(55) Assis, M. C. E.; Cordoncillo, E.; Torres-Mendieta, R.; Beltrán-Mir, H.; Minguéz-Vega, G.; Gouveia, A. F.; Leite, E. R.; Andrés, J.; Longo, E. Laser Induced Formation of Bismuth Nanoparticles. *Phys. Chem. Chem. Phys.* **2018**, *20*, 13693−1396.

(56) Assis, M.; Macedo, N. G.; Machado, T. R.; Ferrer, M. M.; Gouveia, A. F.; Cordoncillo, E.; Torres-Mendieta, R.; Beltrán-Mir, H.; Mínguez-Vega, G.; Leite, E. R.; Sambrano, J. R.; Andrés, J.; Longo, E. Laser/Electron Irradiation on InP Semiconductor: Promising Pathways for in Situ Formation of In Nanoparticles. *Part. Part. Syst. Char.* **2018**, *35*, 1800237.

(57) Machado, T. R.; Macedo, N. G.; Assis, M.; Donãte- Buendia; Mínguez-Vega, G.; Teixeira, M. M.; de Foggi, C. C.; Vergani, C. E.; Beltrán-Mir, H.; Andrés, J.; Cordoncillo, E.; Longo, E.; Beltrán-Mir, H.; Cordoncillo, E.; Andrés, J.; Longo, E. From Complex Inorganic Oxides to Ag−Bi Nanoalloy: Synthesis by Femtosecond Laser Irradiation. *ACS omega* **2018**, *3*, 9880−9887.

(58) Kresse, G.; Hafner, J. Ab Initio Molecular-Dynamics Simulation of the Liquid-Metal−Amorphous-Semiconductor Transition in Germanium. *Phys. Rev. B: Condens. Matter Mater. Phys.* **1994**, *49*, 14251−14269.

(59) Cohen, M. L.; Heine, V. The Fitting of Pseudopotentials to Experimental Data and their Subsequent Application. *Solid State Phys.* **1970**, *24*, 37−248.

(60) Blöchl, P. E. Projector Augmented-Wave Method. *Phys. Rev. B: Condens. Matter Mater. Phys.* **1994**, *50*, 17953−17979.

(61) Monkhorst, H. J.; Pack, J. D. Special Points for Brillouin-Zone Integrations. *Phys. Rev. B* **1976**, *13*, 5188−5192.

(62) Blöchl, P. E.; Jepsen, O.; Andersen, O. K. Improved Tetrahedron Method for Brillouin-Zone Integrations. *Phys. Rev. B: Condens. Matter Mater. Phys.* **1994**, *49*, 16223−16233.

(63) Jónsson, H.; Mills, G.; Jacobsen, K. W. *Nudge Elastic Band Method for Finding Minimun Energy Paths of Transitions* **1997**, 385.

(64) Bader, R. F. W. *Atoms in Molecules: A Quantum Theory*; Claredon Press: Oxford, 1990.

(65) Longo, E.; Avansi, W., Jr.; Bettini, J.; Andres, J.; Gracia, L. *In Situ* Transmission Electron Microscopy Observation of Ag Nanocrystal Evolution by Surfactant Free Electron-Driven Synthesis. *Sci. Rep.* **2016**, *6*, 21498.

(66) Merchan-Merchan, W.; Farahani, M. F.; Moorhead-Rosenberg, Z. Electron Beam Induced Formation of Tungsten Sub-Oxide Nanorods from Flame-Formed Fragments. *Micron* **2014**, *57*, 23−30.

(67) Urbanová, M.; Pokorná, D.; Bakardjieva, S.; Šubrt, J.; Bastl, Z.; Bezdička, P.; Pola, J. IR Laser-Induced Ablation of Ag in Dielectric Breakdown of Gaseous Hydrocarbons: Simultaneous Occurrence of Metastable hcp and Stable fcc Ag Nanostructures in C:H Shell. *J. Photochem. Photobiol., A* **2010**, *213*, 114−122.

(68) Novgorodova, M. I.; Gorshkov, A. I.; Mokhov, A. V. Native Silver and its New Structural Modifications. *Int. Geol. Rev.* **1981**, *23*, 485−494.

(69) Murzakaev, A. M. Size Dependence of the Phase Composition of Silver Nanoparticles Formed by the Electric Explosion of a Wire. *Phys. Met. Metallogr.* **2017**, *118*, 459−465.

(70) Samberg, M. E.; Orndorff, P. E.; Monteiro-Riviere, N. A. Antibacterial Efficacy of Silver Nanoparticles of Different Sizes, Surface Condition and Synthesis Methods. *Nanotoxicology* **2011**, *5*, 244−253.